



## RESEARCH ARTICLE

10.1029/2024MS004313

# Overcoming Set Imbalance in Data-Driven Parameterization: A Case Study of Gravity Wave Momentum Transport

L. Minah Yang<sup>1</sup>  and Edwin P. Gerber<sup>1</sup><sup>1</sup>Center for Atmosphere Ocean Science, Courant Institute of Mathematical Sciences, New York University, New York, NY, USA

## Key Points:

- Unresolved geophysical processes often exhibit long-tail distributions, which leads to imbalanced data sets for data-driven parameterizations
- Two strategies to overcome data imbalance are presented, where either the sampling or loss function is modified to better capture the tails
- Proof of concept is demonstrated by using a wind range metric to improve a machine learning emulator of a physics-based gravity wave parameterization

## Correspondence to:

E. P. Gerber,  
[epg2@nyu.edu](mailto:epg2@nyu.edu)

## Citation:

Yang, L. M., & Gerber, E. P. (2026). Overcoming set imbalance in data-driven parameterization: A case study of gravity wave momentum transport. *Journal of Advances in Modeling Earth Systems*, 18, e2024MS004313. <https://doi.org/10.1029/2024MS004313>

Received 26 FEB 2024  
Accepted 23 DEC 2025

## Author Contributions:

**Conceptualization:** L. Minah Yang, Edwin P. Gerber  
**Data curation:** L. Minah Yang  
**Formal analysis:** L. Minah Yang, Edwin P. Gerber  
**Funding acquisition:** Edwin P. Gerber  
**Investigation:** L. Minah Yang, Edwin P. Gerber  
**Methodology:** L. Minah Yang  
**Project administration:** Edwin P. Gerber  
**Resources:** Edwin P. Gerber  
**Software:** L. Minah Yang, Edwin P. Gerber  
**Supervision:** Edwin P. Gerber  
**Validation:** L. Minah Yang, Edwin P. Gerber  
**Visualization:** L. Minah Yang

© 2026 The Author(s). Journal of Advances in Modeling Earth Systems published by Wiley Periodicals LLC on behalf of American Geophysical Union. This is an open access article under the terms of the [Creative Commons Attribution-NonCommercial License](https://creativecommons.org/licenses/by-nc/4.0/), which permits use, distribution and reproduction in any medium, provided the original work is properly cited and is not used for commercial purposes.

**Abstract** Machine learning for the parameterization of subgrid-scale processes in climate models has been widely researched and adopted in a few models. A key challenge in developing data-driven parameterization schemes is how to properly represent rare, but important events that occur in geoscience data sets. We investigate and develop strategies to reduce errors caused by insufficient sampling in the rare data regime, under constraints of no new data and no further expansion of model complexity. Resampling and importance weighting strategies are constructed with user defined parameters that systematically vary the sampling/weighting rates in a linear fashion and curb too much oversampling. Applying this new method to a case study of gravity wave momentum transport reveals that the resampling strategy can successfully improve errors in the rare regime at little to no loss in accuracy overall in the data set. The success of the strategy, however, depends on the complexity of the model. More complex models can overfit the tails of the distribution when using non-optimal parameters of the resampling strategy.

**Plain Language Summary** Subgrid-scale parameterizations are a part of climate models that represent effects of processes that cannot be directly modeled. In recent years, there have been many efforts to improve upon these parameterizations by applying machine learning (ML) techniques. Since these methods rely heavily on the data set they are learning from, it is important to consider the frequency at which important events occur within the data set because they are adept at learning frequent events at high accuracy but are prone to learning rare but important events at low accuracy. To remedy this *data imbalance* problem, we developed a resampling methodology that can be easily adjusted by tuning just two parameters. We find that a right combination of those parameters can improve the accuracy of an ML model at the rare event regime while keeping the accuracy high in the frequent regime. However, a “wrong” combination can actually increase the errors at the rare event regime by overfitting to that regime.

## 1. Introduction

Machine learning techniques have been used to develop data-driven parameterization of un- or under-resolved processes in climate models, including a comprehensive representation of all missing terms, either at once (Brenowitz & Bretherton, 2019) or separately (Yuval et al., 2021), or specific processes, including gravity wave (GW) momentum transport (Chantry et al., 2021; Espinosa et al., 2022) and radiative transfer (Ukkonen, 2022). None of these attempts yielded a perfect subgrid-scale model, begging a general question: what can one do to improve a given data-driven parameterization? As these processes, and geoscience data sets more generally, are often high-dimensional and exhibit long-tailed distributions, a common problem is to properly learn rare and extreme events. This is particularly problematic if these extreme events have an outsized impact on the climate, or become more prevalent in a changing climate. How can we capture important but rare events from the tail of the distribution as best as possible given the data set available to us? This is a data imbalance problem, and we propose strategies to combat it in this paper.

Set imbalance is a common challenge in machine learning (ML). In binary classification, the imbalanced data set problem refers to a skewed distribution of the two target classes in a data set. A naive learning algorithm will inherit an asymmetric class representation in the data set, and will typically produce classifiers that predict the minority class with lower accuracy than it does for the majority class. These biased classifiers prove even more problematic when the minority class holds more importance or utility. As this combination of challenges is

Writing – original draft: L. Minah Yang  
Writing – review & editing:  
L. Minah Yang, Edwin P. Gerber

ubiquitous in real data sets, many methods that curb and minimize biases that stem from imbalanced data sets have been developed, as reviewed by He and Garcia (2009) and Krawczyk (2016).

Data imbalance poses difficulties for ML tasks outside of binary classification. While it is straightforward to extend methods for treating imbalanced data sets for binary to multi-class classification, it has proven more difficult to extend this for regression tasks. Here, one seeks to learn a function  $g$  from a set of inputs  $\vec{x}$  to outputs  $\vec{y}$  where the example pairs  $(\vec{x}, \vec{y})$  is unevenly distributed. As with the classification problem, the task is particularly hard if we care especially about the behavior of  $g$  for rare pairs of  $(\vec{x}, \vec{y})$ .

In this paper, we explore systematic methods for overcoming data imbalance in regression tasks, illustrating them with a case study of data-driven parameterization GW momentum transport. Gravity waves play an important role in forcing the large scale atmospheric circulation, but their small scale makes them challenging to properly represent directly. We seek a function  $g$  that maps vertical profiles of the resolved wind, temperature, and GW source information within a column of an atmospheric model:  $\vec{x}$ , to the profiles of the grid scale momentum tendency by unresolved gravity waves associated with this large scale environment:  $\vec{y}$ . We assume limited resources, in that one cannot simply increase the size of the data set or complexity of our model  $g$  to overcome the problem: the goal is to work with the data and model one has on hand.

First steps have been taken towards deriving data-driven schemes for GWs by exploring how well ML approaches can emulate existing, physics-based parameterizations (Chantry et al., 2021; Sun et al., 2023). Both studies found that data imbalance was challenging, particularly for capturing the momentum forcing by GW excited by orography. Not only are most grid cells of a GCM flat, but even where there is topography, the waves themselves are highly intermittent. Here, we will focus on non-orographic waves, but the method is general and an ad hoc version of it was used by Sun et al. (2023) to emulate an orographic parameterization. More specifically, we build on the work of Espinosa et al. (2022), who emulated a physics-based GW parameterization (GWP) scheme (Alexander & Dunkerton, 1999) hereafter referred to as AD99, with a deep neural network (NN) architecture called WaveNet. We continue this investigation to illustrate our approach for improving a generic ML methodology. Exploring our method in the context of emulation also allows us to explore the ability of a scheme to generalize to different climates.

The strategy involves two distinct steps. First, one must identify the data imbalance. This requires “domain knowledge” of the problem, to identify key metric(s) that quantify rare cases where errors in the data-driven scheme limit its effectiveness. As detailed in Section 2, we establish a wind range metric to identify rare cases where WaveNet emulator systematically fails. On top of being rare, these are cases where the physics of AD99 scheme become more non-local, and so more challenging to learn.

Once the data imbalance is identified, the second step is to treat it during model training and implementation, as detailed in Section 3. We illustrate two strategies at the learning stage, either to modify the sampling of training examples so that rarer cases are better represented from the start, or to leave the distribution as it is, but adjust the loss function to more strongly penalize mistakes on the rare cases. To construct a principled method for this rebalancing, we borrow a concept from histogram equalization: a linear interpolation of the original distribution to a more uniform distribution parameterized by a scalar  $t$  which can be varied from 0, where no change is made, to 1, where the distribution is made completely uniform. The goal is to improve representation of the rare cases without losing skill on the central part of the distribution or overfitting the data in the tails, and the parameter  $t$  allows one to calibrate the degree of rebalancing.

These strategies assume that the ML model has enough complexity to learn the complex nonlinear behavior described by physics of  $g$ , but the data imbalance encourages the model to ignore rare samples and predominantly learn from the typical samples. As we'll show in Section 4.2.2, overfitting can occur when the ML method is too complex with respect to the amount of training data available. In addition to improving the training of an ML scheme, one can mitigate data imbalance by applying a bias correction at the inference stage. This involves computing the mean bias of the ML model as a function of the relevant metric (the wind range in our case study of GWP emulation), and subtracting the bias from the output.

The remainder of the paper is structured as follows. Section 2 illustrates how we identified data imbalance, Section 3 details modified training and bias removal methods to overcome this imbalance. Our case study is presented in Section 4. To demonstrate the generality of the method, we also introduce an alternative ML strategy,

an Encoder-Dense-Decoder (EDD). We use our approach to improve both WaveNet and EDD. Furthermore, we illustrate how our approach can fail when the complexity of the ML method exceeds the data available, leading to overfitting. Section 5 concludes our study and outlines possible future directions for this research.

## 2. Identifying Data Imbalance

A first step towards improving a data-driven parameterization—or more generally, any data-driven task—is to identify potential imbalances in the training set. This process requires detailed knowledge of the application, as one is searching for metrics to quantify rare cases that are important for the performance of the task. The process is straightforward in low dimensional data sets, that is, if one needs to differentiate cats from dogs, are the animals evenly distributed in the example data, but quickly becomes difficult in high dimensional data sets. Here, we illustrate an example where the input data has 83 dimensions, but we seek a projection onto a 1D subspace that clearly identifies rare, but important, samples that need to be learned.

Our goal is to improve a data-driven emulator of the single column AD99 GW parameterization, as implemented in the Model of an idealized Moist Atmosphere, MiMA (Garfinkel et al., 2020), following the work of Espinosa et al. (2022). We direct the reader to Alexander and Dunkerton (1999) for details on the parameterization and Espinosa et al. (2022) and Garfinkel et al. (2020) for details on the atmospheric model, but briefly review the most salient points here.

As in Espinosa et al. (2022), we use an integration of MiMA at triangular truncation T42 resolution (corresponding to a  $\approx 3^\circ$  grid) with model parameters configured to produce a realistic representation of northern hemisphere climate by Garfinkel et al. (2020). The model is integrated for 60 years, and after discarding the first 20 years' data as spin-up, we use years 21–30 for the training and years 56–60 for the validation set. Output from the model is saved 4 times a day, yielding over  $1.1 \times 10^9$  samples, where each sample consists of vertical profiles of winds and temperature (the inputs), one for each column on a  $128 \times 64$  longitude-latitude grid, and the parameterized GW tendency as the output. For simplicity, we focus only on the zonal (East-West) GW tendencies.

AD99 is a multi-wave GW parameterization that adheres closely to the scheme established by Lindzen (1981), which assumes the conservation of wave action flux and wave-mean flow interactions under linear theory. The scheme determines GW momentum transport by launching a spectrum of non-interacting, monochromatic waves. Thermodynamic breaking criteria determine when each wave breaks and deposits its momentum into the mean flow: waves tend to break when they near a critical level, where the speed of the large scale winds equals that of the GW, or when their amplitude becomes sufficiently large to overturn. This latter criteria is favored at upper levels where density decays. Additional criteria account for waves that would be filtered out at the source level (the nominal tropopause) or reflected downward. Important for our application, momentum carried by waves that do not break before reaching the model top are deposited in the upper levels of the column, thereby preventing a leak of momentum through the model top (Shaw et al., 2009). A key simplification of the scheme is that the source spectrum is only a function of latitude, meant to capture a simple background of waves generated by convection, frontogenesis, and orography.

We first looked for variations in the accuracy of our data-driven emulators as a function of location and time of year. With orographic GW drag, the skewed distribution of the surface roughness generates data imbalance, as explored by Sun et al. (2023). The source spectrum in this configuration of the AD99 scheme is nearly uniform, however, and there were no significant variations in the mean error rates.

We next explored how changes in meteorological conditions (winds and stratification) could lead to data imbalance. By varying the input features to a NN based emulator, Espinosa et al. (2022) found that zonal and meridional winds were by far the most important predictors. Feature importance analysis by Connelly and Gerber (2024) confirmed that wind profile is most important, particularly in the vicinity of the prediction level, as critical level filtering is the dominant mechanism for GW breaking in the scheme.

Physical intuition can be garnered from Figure 1, which shows two example wind profiles from an integration of the MiMA in the left panel, and the momentum tendency computed by AD99 in the center. The blue profile exhibits a more typical case; we will define “typical” precisely below. Critical line wave breaking leads to deposition of easterly momentum in easterly shear zones, for example, near 100 hPa, and conversely westerly momentum in westerly shear zones, for example, near 1 hPa. The orange profile demonstrates a less typical case

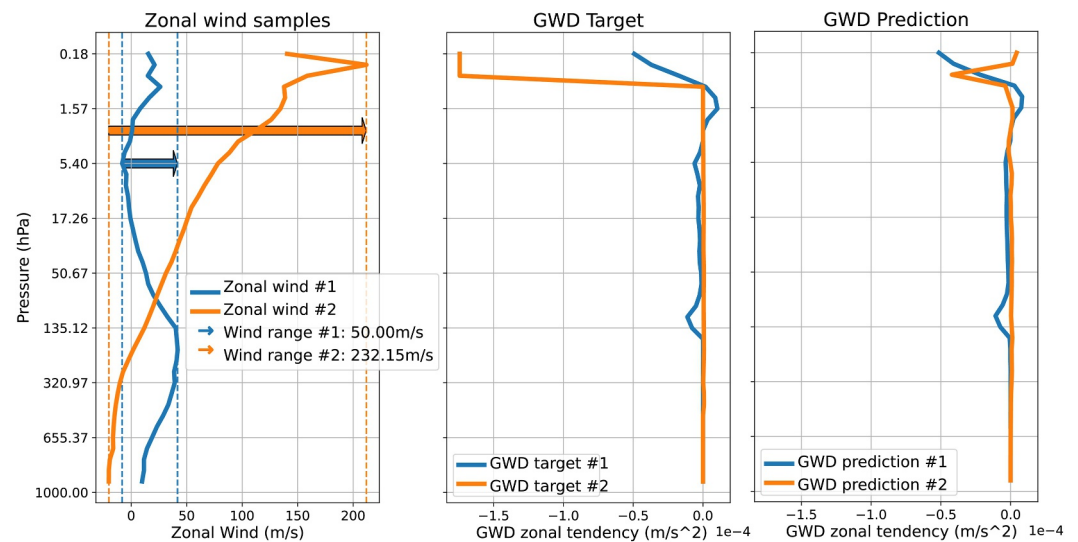


**Figure 1.** (left) Two zonal wind profiles sampled near the South Pole at different times in the control integration. (middle) The physics-based (AD99) computation of gravity wave momentum deposition (GWD) associated with these two profiles in the left panel. (right) The GWD output by the WaveNet emulator of AD99 for the same input profiles.

with easterly flow in the troposphere below strong westerly shear throughout the atmospheric column. Westerly waves are filtered out by easterly winds at the source level (hence no westerly forcing), but the easterly half of the spectrum never experiences critical levels. The scheme thus deposits them all near the model top.

The right panel of Figure 1 provides anecdotal evidence that the WaveNet emulator does a reasonable job of capturing the momentum tendencies from the more typical blue profile case, but fails rather spectacularly with the orange profile. As detailed by Connelly and Gerber (2024), WaveNet is good at capturing critical level behavior, but struggles to capture non-local effects on the momentum tendencies, both the impact of source level filtering and integrated behavior, where an absence of easterly shear allows waves to reach the top.

We hypothesize that WaveNet’s emulation of AD99 in MiMA suffers from data imbalance, in that GW breaking is most often associated with local critical levels. WaveNet learns this relationship well. Cases where the momentum forcing depends on non-local behavior (e.g., when surface level filtering or low level critical levels remove part of the spectrum low in the atmosphere, or when a lack of critical levels leads to momentum deposition near the model top) are more seldom seen, and so tend to be poorly captured the data-driven scheme. The challenge is to translate this physical intuition into an objective metric to identify the rarer cases dominated by non-local effects. The input space is 83 dimensional (zonal wind  $\vec{u}$  and temperature  $\vec{T}$  at 40 levels each, plus surface pressure, latitude, and longitude), but we want a single metric to sort the data. After significant trial and error we developed a simple “wind range” metric that captures many of these rare cases.

The wind shear is a crucial quantity in computing GW forcing on the mean flow. Large shear at any given level favors wave breaking, as GWs over a wider range of phase speeds will experience a critical level. Profiles with large shear, particularly at lower levels, tend to exhibit non-local behavior, as the GW spectrum is rapidly depleted, rendering upper level critical levels moot. (This is to say, a second shear zone will not be associated with GW breaking because waves have already broken below.) In addition, strong shear in one direction can lead to cases like that exhibited in Figure 1, where the momentum conservation criterion leads to momentum tendencies near the model top, even if individual waves wouldn’t otherwise break there. An admittedly crude proxy metric we consider to represent the overall presence of shear is the wind range, the total span of winds throughout the atmospheric column. Formally,

$$\text{wind range} = \left( \max_{i=1, \dots, n_{\text{lev}}} u_i \right) - \left( \min_{i=1, \dots, n_{\text{lev}}} u_i \right). \quad (1)$$

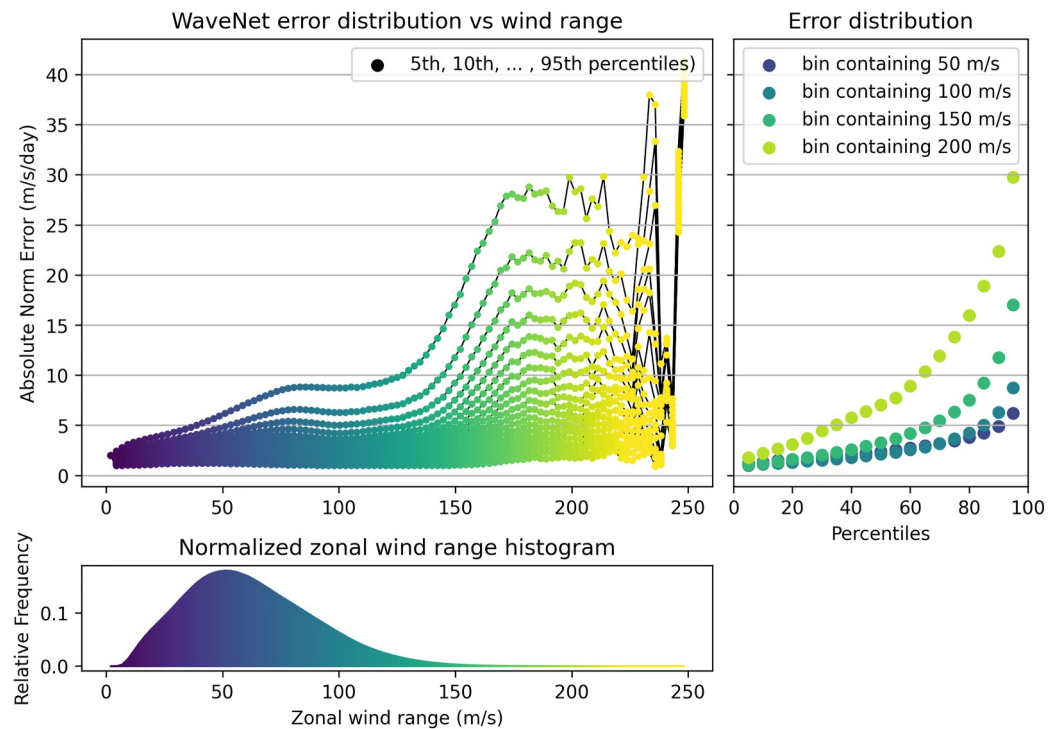


**Figure 2.** Bottom panel shows the histogram of the data set where each sample is represented by its zonal wind range (Equation 1). Frequency is the number of samples in a bin relative to the total number of samples. Top left: For each of the 100 equal-width bins of the histogram, we show 5th to 95th absolute error percentiles at 5-percentile increments. Thus we can view the error spread as a function of wind range. Due to noisy error statistics for samples with wind range  $>200$  m/s, we exclude those samples in the analysis in the following sections. Top right: The error percentiles for a select few bins show that larger errors are incurred more often as the wind range increases.

The wind range metric is illustrated by the arrows in the left panel of Figure 1. It suggests that WaveNet may struggle when the wind range is large (the orange profile). While this metric was motivated by the physical argument that these high shear cases are more challenging to learn due to non-local effects, Figure 2 shows that these high wind range cases are rare as well.

The wind range exhibits the two key features of data imbalance. First, the input data exhibits a long-tailed distribution with respect to the wind range, and second the ML based emulator systematically struggles with the tail of this distribution. This is most clearly illustrated in Figure 2, which shows the distribution of errors for different values of the wind shear. The spread of error increases superlinearly with respect to wind range. For profiles with a wind spread of 50 m/s, at the mode of the distribution, the error is the prediction of the drag is less than 5 m/s/day for over 90% of cases. For profiles with range of 100 m/s, the error rates are only modestly worse, 85% of profiles exhibit an error less than 5 m/s/day. The percentage of profiles with errors less than 5 m/s/day decreases to 70% and 30% for profiles with wind ranges 150 and 200 m/s, respectively. Error rates at the 90th percentile are associated with 16 and 28 m/s/day, respectively, a full three to five times worse for cases at the mode of the distribution.

Figure 2 motivates another, even simpler approach of addressing data imbalance: bias removal. The high absolute error rates for rare profiles with large wind range are in part associated with systematic mean biases in the prediction (not shown). In general, a well-trained ML scheme will have no bias in the overall mean, but it can systematically under and over-predict profiles with respect to metrics like the wind range. For example, it may trivially under-predict the GW tendencies over the main part of the distribution, but massively over-predict the tendencies at the tail. As discussed in Section 3.3 one can remove these biases at the time of inference.

For the remainder of the paper, we use the wind range metric, and the data imbalance it reveals, to improve the training and implementation of WaveNet and a related ML scheme. These methods are generic, and ready to apply once a user has identified the metric to quantify the imbalance. The better one can sort prediction errors in a high

dimensional data set along a single (or at least a small number of) dimension(s), however, the better one is positioned to use these strategies to improve the scheme.

### 3. Treating Data Imbalance

Our goal is to help the data-driven scheme perform better on the tails of the distribution *without* decreasing performance over the main part of the distribution. This makes the typical balancing act between “bias” and “variance” that one seeks with any ML task more challenging. Good performance requires a scheme that both learns the training data well (has low bias) and works equally well on new data (has low variance). By this, we mean that the skill is uniform for different samples from the underlying distribution, so it generalizes well to new inputs it has not seen before.

A large bias is associated with under-fitting, where the method lacks enough training data and/or expressivity to capture the relationships, while a large variance is associated with over-fitting, where the ML scheme uses “noise” (unimportant features) in the training data to reduce the bias. This is a case of having too much expressivity relative to the amount of data. The expressivity of a ML scheme is related to its complexity (roughly, the flexibility it has to identify relationships between inputs and outputs, which is a function of both the method and the number of free parameters it is given). For our application, we are given some ML scheme of fixed complexity (i.e., WaveNet). We must ensure there is still enough training data in the center of the distribution to avoid under-fitting it, and not too much emphasis on the tails to cause over-fitting.

Learning from unbalanced data sets is challenging. For example, consider a data set where 99% of the data set is class A and the remaining 1% is class B. A binary classifier that always predicts class A can still be considered very good under a seemingly innocent metric such as average accuracy, defined as

$$\text{average accuracy} \equiv \frac{\text{\#correctly labeled samples}}{\text{\#of total samples}},$$

with a value of 0.99, although it completely fails to learn the characteristics of class B. Methods to remedy difficulties attributed to imbalanced data sets for classification are far and plenty (He & Garcia, 2009; Johnson & Khoshgoftaar, 2019), and are used in a variety of applications including object detection (Oksuz et al., 2021).

These methods can be broadly categorized into data-level, algorithm-level, and the hybrid of those two. Data-level methods manipulate the distribution of the training data distribution: such as undersampling from the majority class and oversampling from the minority class (Chawla et al., 2004), or generating synthetic samples of the minority class (Chawla et al., 2002) through randomly weighted linear combinations of samples. Algorithm-level methods adjust the learning algorithm to increase/decrease the impact of samples from minority/majority class. The latter case falls under cost-sensitive learning as it is implemented by imbuing a cost or penalty term in the learning process (Elkan, 2001; Krawczyk, 2016).

Rare event sampling is another technique related to treating data imbalance that has been applied to geoscience data sets. For example, Webber et al. (2019) uses histogram-based data rebalancing techniques in quantile diffusion Monte-carlo, a rare-event sampling technique, to generate samples of extreme storms. However we are not aware of efforts that successfully use samples generated by rare-event sampling for inference, and therefore leave it out of the discussion below.

Although many methods for treating data imbalance are established for classification, extending them for regression is nontrivial. There have been some efforts on this front as done by Torgo et al. (2015), Ding et al. (2019), and Rudy and Sapsis (2023). Torgo et al. (2015) extends the Synthetic Minority Oversampling TEchnique (SMOTE; Chawla et al., 2002) to regression by assuming near linearity of the model being learned, Rudy and Sapsis (2023) extends relative entropy based loss functions from scalar outputs to low dimensional vector outputs, and Ding et al. (2019) proposes a new loss function and a model design that memorizes extreme events for time series applications. Some shortcomings of these solutions are that they are incompatible with nonlinear problems and difficult to implement in applications with high dimensional data sets.

We prepare two methods to address data imbalance in regression tasks. Both methods require first identifying a metric along which the high-dimensional data set yields a long-tailed distribution; in our case, the wind range. We

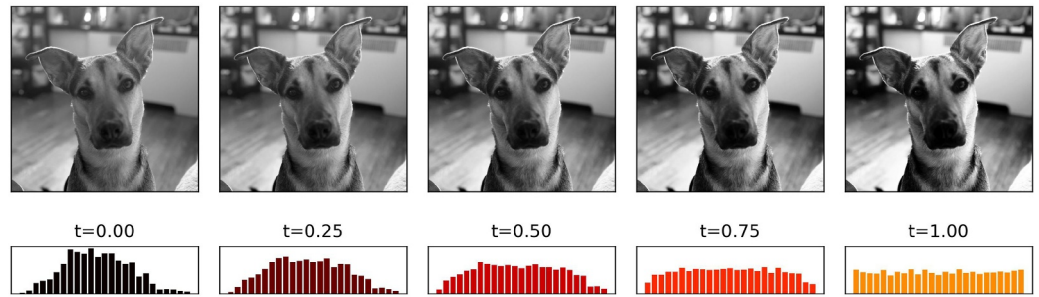


**Figure 3.** An example of histogram equalization performed for image processing with  $t$  ranging from 0 to 1. The original image corresponds to  $t = 0$ . As  $t$  increases, moderate saturation pixels are pushed towards their nearest extremes. At  $t = 1$ , the pixels are distributed almost uniformly.

project our high-dimensional data set to the low-dimensional space identified by the metric. Section 3.1 shows how histogram equalization can be applied to transform unbalanced distribution to one more uniform. This idea is closely related to transportation theory (optimal transport), which is the study of allocation of resources with a constraint of cost appended to the transportation of those resources. Since we merely intend to modify the data distribution encountered by the training algorithm, rather than to transform the data itself, we drop the transportation cost constraint. In Section 3.2, we describe the data rebalance method, which extends the ideas of over/undersampling methods to treating data imbalance for regression tasks by applying linear transformations to the probability distribution function (PDF) of the data set. Finally, we describe mean bias removal in Section 3.3.

### 3.1. Histogram Equalization

Histogram equalization is an image processing method that adjusts the contrast of an image by changing the shape of the histogram of the intensity values, and is the simplest optimal transport method for 1D data. The extent to which the shape of the histogram is modified is parameterized by  $t \in [0, 1]$  where  $t = 0$  yields the original histogram, and  $t = 1$  a target histogram. By equalization, we aim for a target distribution that is uniform, with an equal number of pixels in each intensity bin.

Figure 3 shows an example of this applied to a grayscale image where each sample has a value in  $[0, 1]$  which represents a greyscale value between black and white. The original histogram ( $t = 0$ ) has the majority of pixels in the moderate intensity region, and very few pixels are close to minimum and maximum intensities. As the parameter  $t$  increases to 1, the distribution is flattened in the peak region and elevated in the extreme regions. Lighter pixels are made lighter and darker pixels are made darker, qualitatively yielding images with greater contrast as  $t$  increases.

Let us describe this procedure in more detail. Let  $x_i$  denote the intensity of the  $i$ th pixel of an  $m \times m$  image, and let permutation  $\sigma$  be defined such that  $\{x_{\sigma(j)}\}_{j=1}^{m^2}$  are sorted in increasing order,

$$x_{\sigma(1)} \leq \dots \leq x_{\sigma(m^2)}.$$

Assign  $\{y_j\}_{j=1}^{m^2}$  to the cumulative distribution function (CDF) of the target distribution. This corresponds to  $m^2$  equispaced, ordered nodes from 0 to 1 since the target is the uniform distribution for histogram equalization:

$$y_j = (j - 1)/(m^2 - 1), \quad j = 1, \dots, m^2.$$

In general, the CDF of any desired target distribution suffices as the values of  $y_j$ 's. Then, the new intensity value for the  $i$ th node is given by

$$z_i := (1 - t)x_i + ty_{\sigma^{-1}(i)}. \quad (2)$$

Here is a numerical example of applying this to a  $2 \times 2$  image. The original image is given by pixels

$$\begin{bmatrix} x_1 & x_2 \\ x_3 & x_4 \end{bmatrix} = \begin{bmatrix} 0.60 & 0.52 \\ 0.25 & 0.44 \end{bmatrix}.$$

The sorting permutation is  $\sigma = [3, 4, 2, 1]$  for a row-wise uncoiling of the matrix, and the target values are  $y_1 = 0$ ,  $y_2 = 1/3$ ,  $y_3 = 2/3$ ,  $y_4 = 1$ . Thus, the transformation yields

$$\begin{bmatrix} y_{\sigma^{-1}(1)=4} & y_{\sigma^{-1}(2)=3} \\ y_{\sigma^{-1}(3)=1} & y_{\sigma^{-1}(4)=2} \end{bmatrix} = \begin{bmatrix} 1 & 2/3 \\ 0 & 1/3 \end{bmatrix}$$

for  $t = 1$ , and the general formula for any  $t \in [0, 1]$  is given by

$$(1-t) \begin{bmatrix} x_1 & x_2 \\ x_3 & x_4 \end{bmatrix} + t \begin{bmatrix} y_4 & y_3 \\ y_1 & y_2 \end{bmatrix} = (1-t) \begin{bmatrix} 0.60 & 0.52 \\ 0.25 & 0.44 \end{bmatrix} + t \begin{bmatrix} 1 & 2/3 \\ 0 & 1/3 \end{bmatrix}.$$

### 3.2. Data Rebalancing

Our goal is to change the distribution of the training data set while taking full use of the available data and without generating synthetic data. Histogram equalization for image processing achieves the reshaping of the data set distribution by transforming the values of the sample from  $x_i$  to  $z_i$  as shown in Equation 2. Doing so may move a sample from one histogram bin to another, thereby changing the histogram directly. Our method uses the linear mapping from the original to the new intensity values described in Equation 2, but apply the mapping to the PDF instead. The newly assigned probability may increase or decrease a sample's contribution to the training process. We describe the method in detail below, and propose two implementations of the method in Sections 3.2.1 and 3.2.2, respectively.

Let  $H^{(0)}$  be the histogram of the training data set  $X_{\text{training}}$  with  $N$  bins,

$$\{[b_0, b_1], \dots, [b_{N-1}, b_N]\}.$$

The count of samples in the  $n$ th bin,  $[b_{n-1}, b_n)$  is  $h_n^{(0)}$ , and the ideal count of the samples in the  $n$ th bin in the ideal histogram is  $h_n^{(1)}$ . Here, the ideal histogram is uniform with  $N$  equal width bins, so  $h_n^{(1)} = M/N$  for all  $n = 1, \dots, N$  for a data set with  $M$  samples. The new count of the  $n$ th bin for parameter  $t$  is then:

$$h_n^{(t)} = (1-t)h_n^{(0)} + th_n^{(1)}. \quad (3)$$

Since the  $n$ th bin originally represented  $h_n^{(0)}/M$  of the training set and now we want it to represent  $h_n^{(t)}/M$  of the training set, the ratio between the two determines the resampling rate in the  $n$ th bin.

$$\alpha_n^{(t)} := \begin{cases} h_n^{(t)}/h_n^{(0)} = (1-t) + th_n^{(1)}/h_n^{(0)} & , h_n^{(0)} > 0 \\ 0 & , h_n^{(0)} = 0 \end{cases} \quad (4)$$

These ratios determine the new sampling rates for the training data. We found in practice that fairly low  $t$ -values still yielded very large  $\alpha$  ratios at bins belonging to the extreme tail of the distribution. To avoid unreasonable resampling rates being assigned to rare data points (see Section 4.2.1 for more discussion), we bound the ratios by the maximum repeat parameter as shown in Equation 5,

$$\tilde{\alpha}_n^{(t)} := \begin{cases} \min\{\alpha_n^{(t)}, \text{max\_repeat}\} & , h_n^{(0)} > 0 \\ 0 & , h_n^{(0)} = 0. \end{cases} \quad (5)$$

Thus, the final resampling rate,  $\tilde{\alpha}_n^{(t)}$ , is determined by three decisions: (a) choice of histogram bins; (b)  $t$ , the linear mapping parameter; and (c) the maximum repeat parameter. The resampling strategy is no longer a simple bilinear

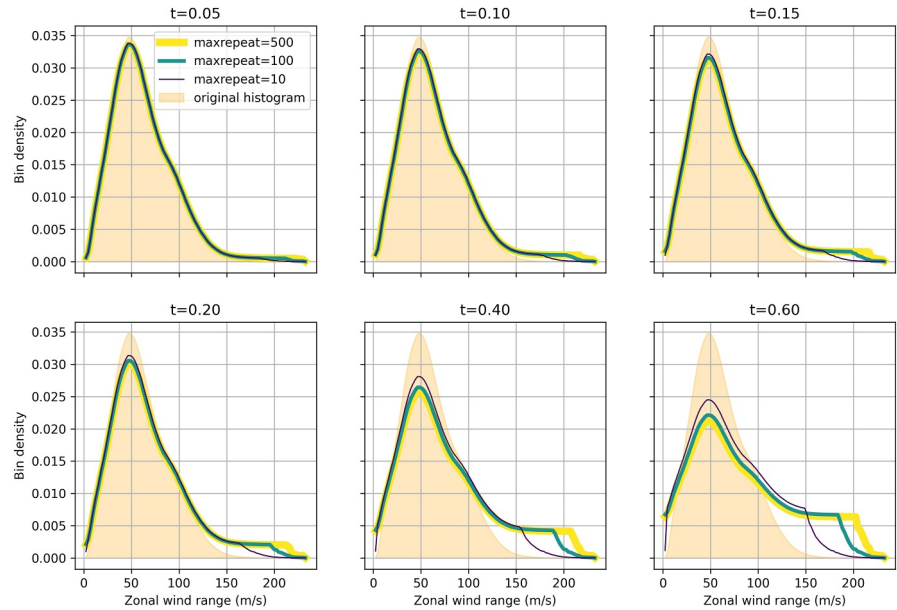


**Figure 4.** Each of the panels correspond to  $t$  values ranging from 0.05 to 0.60. The 3 lines for each panel represent the impact of  $\text{maxrepeat}$  parameter values 10, 100, and 500. The original histogram is shown filled in as a basis for comparison.

interpolation between the original ( $h^{(0)}$ ) and desired ( $h^{(1)}$ ) histograms due the maximum value of the resampling rate. The counts for the bins of the new, resampled histogram for some  $t \in [0, 1]$  and  $\text{max\_repeat}$  is,

$$\tilde{h}_n^{(t)} = \tilde{\alpha}_n^{(t)} h_n^{(0)}. \quad (6)$$

The process is easier to visualize than spell out: Figure 4 shows the original normalized histogram,  $h^{(0)}$ , plotted in foreground with the new histograms,  $\tilde{h}^{(t)}$ , with increasing values of  $t$  for each panel, as well as three different values for  $\text{max\_repeat}$  in each panel. The impact of  $\text{max\_repeat}$  is amplified for larger values of  $t$ , and can be seen most clearly in the bottom three panels. Smaller  $\text{max\_repeat}$  values initiate sharp decays of probability density at smaller wind range values, and redistribute weight away from the tail.

The number of histogram bins was kept constant here. It governs how finely one resolves the distribution. One could also allow the width of the bins to vary, say to more finely capture the center versus the tails. Coarser bins, on the other hand, allows one to increase the value of  $t$  without oversampling the tail as extremely. This approach was taken by Sun et al. (2023), who effectively implemented our method with  $t = 1$ , but with only 20 bins.

### 3.2.1. Implementation I: Direct Sampling

State-of-the-art optimization methods for deep neural networks rely on incremental, iterative updates of the model weights. They are incremental in that each update is based only a subset of the training data set called a *batch*, and iterative in that the training data set is passed through the optimization method many times before the model weights converge to an acceptably optimal state. An *epoch* is a measure of unit for the progress of the training of a model defined by a single pass over the training data set, for which each sample in the training data set processed exactly once. Since our strategy changes the contribution of each sample to the training algorithm based on where in the data distribution the sample belongs, some samples will be seen more often than others. Therefore, we modify the definition of an epoch to mean a single-pass over a resampled subset of the data set. We outline the procedure for resampling in context of a general NN training algorithm, which is written as a pseudoalgorithm (Algorithm 1) in Appendix A.

First, compute resampling rates  $\tilde{\alpha}_n^{(t)}$  for each bin using Equation 5. Next, for each bin labelled by  $n = 1, \dots, N$ , resample and collect the indices of the chosen samples. If  $\tilde{\alpha}_n^{(t)} < 1$ , then it is straightforward to sample from the  $n$ th

bin with probability  $\tilde{\alpha}_n^{(t)}$  by randomly choosing a subset of the bin of size  $\tilde{h}_n^{(t)}$  without replacement. Another method is to sample from the uniform distribution  $h_n^{(0)}$  times and keep the indices that correspond to sampled values less than  $\tilde{\alpha}_n^{(t)}$ . For both methods, the selected indices are recorded. On the other hand, if  $\tilde{\alpha}_n^{(t)} > 1$ , then include every sample from this bin  $\text{floor}(\tilde{\alpha}_n^{(t)})$  times, and then sample with probability  $\tilde{\alpha}_n^{(t)} - \text{floor}(\tilde{\alpha}_n^{(t)})$ . Following good practice, the collected indices from all  $N$  bins should be combined, shuffled, and separated into batches. These batches should then be fed to the training algorithm, which will update the NN model weights once for each batch.

Once all of the batches are processed and if further training is needed, repeat the resampling step to select another realization of the new data distribution. Note that every iteration of resampling is done without replacement, but samples may be repeated from one iteration to the next. It is straightforward to include an additional step to resample at the next iteration without replacement by keeping track of which samples and how many times those had been picked in previous iterations. When sampling without replacement is implemented across epochs, all of the samples to be seen by the training algorithm at least once after  $\text{ceiling}((\min_n \tilde{\alpha}_n^{(t)})^{-1})$  epochs. We include a pseudoalgorithm for the resampling method in Algorithm 2 in Appendix A.

### 3.2.2. Implementation II: Weighted Loss Function

An alternative implementation of our approach is to modify the loss function to account for disparity in the distribution. Success in training deep NNs are attributed to efficient back-propagation, a method of updating model weights with the goal of minimizing a loss computed from a batch of samples. Since loss functions are typically defined for a single pair of the target and the predicted value, the loss over a batch of samples is an average of the loss function values for each of the samples in that batch. This implies that every sample in the batch has equal importance in updating the model weights. Our resampling strategy aims to modify the data distribution to lend importance to some samples and reduce impact from other samples. We propose using a weighted average in the accumulation of loss function values of a batch, where the weight for each sample corresponds to the resampling rate of the bin the sample belongs to. For a sample indexed by  $i$  that belongs to bin  $n$ , the weight is determined by parameters  $t$  and `max_repeat` via Equation 5:  $w_i \equiv \tilde{\alpha}_n^{(t)}$ . The weights can be computed for the entire training data set prior to any training and passed to the training loop to compute a weighted average of the loss function for each batch, as shown in Section 3.2.2.

$$\text{Loss}_{\text{avg}} \left( \{y_i\}_{i=1}^{\text{batch size}}, \{\hat{y}_i\}_{i=1}^{\text{batch size}} \right) = \frac{1}{\text{batch size}} \sum_{i=1}^{\text{batch size}} \text{Loss}(y_i, \hat{y}_i) \quad (7)$$

$$\text{Loss}_{\text{weighted avg}} \left( \{y_i\}_{i=1}^{\text{batch size}}, \{\hat{y}_i\}_{i=1}^{\text{batch size}} \right) = \frac{1}{\text{batch size}} \sum_{i=1}^{\text{batch size}} w_i \text{Loss}(y_i, \hat{y}_i). \quad (8)$$

### 3.2.3. Maximum Repeat: Fail-Safe Against Overfitting

The maximum repeat parameter, Equation 5, puts a threshold on the oversampling rate to prevent overfitting. This allows us to fine tune treatment of the data imbalance by relaxing the computed resampling rates of bins with high  $\alpha$  ratios, which typically occur at the extreme tail of the distribution. By limiting how much importance is given to the extreme tail, this parameter helps redistribute some weight back to the rest of the distribution. This allows the user to fine tune which span of the tail is most affected by rebalancing.

### 3.3. Bias Removal

In addition to the resampling method, we propose a correction method to be employed at time of inference to further enhance the quality of the ML model. This method applies a first-order correction to remedy the bias of a trained model, where the bias is computed along the metric used to identify the data imbalance. There are a couple of ways to compute the bias. Consider a data set of  $M$  samples that were binned into  $N$  bins where  $B_n$  is the set of indices of samples that belong to the  $n$ th bin. The output variable has dimension  $d$ , and we denote the target and predicted variable of the  $i$ th sample by

$$\vec{y}_i = \begin{bmatrix} y_{i,1} \\ \vdots \\ y_{i,k} \end{bmatrix}, \vec{\hat{y}}_i = \begin{bmatrix} \hat{y}_{i,1} \\ \vdots \\ \hat{y}_{i,k} \end{bmatrix}$$

where  $\hat{\cdot}$  is used to denote the ML predictions. The mean error profile for the entire data set can be computed by

$$\text{mean error profile} = M^{-1} \sum_{i=1}^M \vec{y}_i - \vec{\hat{y}}_i.$$

For a well trained scheme, the mean error profile should be close to a vector of zeros. Similarly, we can compute the mean error profile for each bin,

$$\text{mean error profile for bin } n = \left\{ \left| \mathcal{B}_n \right|^{-1} \sum_{i \in \mathcal{B}_n} \vec{y}_i - \vec{\hat{y}}_i \right\}_{n=1}^N. \quad (9)$$

Large errors in bins of the tails can be balanced by smaller errors in the fat tail of the distribution. At inference, we simply determine the bin the sample belongs to and subtract the appropriate mean bias profile.

#### 4. Case Study: Data-Driven GWP Emulation

Section 4.1 describes two model architectures we use to test our method: WaveNet from Espinosa et al. (2022) and a convolutional NN encoder-dense-decoder (EDD). Both implementations of the data rebalancing, with varying  $t$  parameters, are applied during training on the same MiMA data set. Offline results are presented in Section 4.2, and the emulators with the best offline results are tested online in Section 4.3. Online refers to replacing AD99 within MiMA integrations with our trained ML emulators.

##### 4.1. Model Architectures

We include a short summary of WaveNet here, and refer readers to Espinosa et al. (2022) for a full description. WaveNet takes in a concatenation of all of the input variables and applies several dense layers that split into pressure level-specific “branches.” The branches themselves are also dense layers that output GWD values for a specific pressure level of the MiMA vertical grid, and do not communicate with one another.

The EDD architecture uses 1D convolutional layers in the encoder and decoder sections and dense layers in the middle section. This structure is imposed to encourage the model to learn local interactions in the encoder section via convolutions while downsampling layers compress the outputs. This combination of convolutional layers followed by downsampling is commonly used in autoencoders, which can serve as a nonlinear dimension reduction technique that extract essential information. The middle dense section allows the processing of global relations and the decoder section reassembles the vertical profile of the zonal GW drag with transposed convolutions and upsampling. Additional details are included in Appendix B.

The hyperparameters for these architectures, listed in Table 1, include the number and width of the dense layers, the number of (transposed) convolution layers and the size and number of filters for each of these (transposed) convolution layers. Some degrees of freedom were removed by restricting the encoder and decoder halves to be as symmetric as possible, while accounting for the fact that the encoder receives multiple channels and the decoder outputs a single channel. For the remaining degrees of freedom, we used RayTune (see Liaw et al. (2018)) to thoroughly tune the hyperparameters. We contrast two sizes for each architecture: a smaller network of approximately 350,000 parameters; and a larger network of approximately 700,000 parameters. Espinosa et al. (2022) found that large networks yielded better offline skill than their smaller counterparts, but at the expense of additional computational costs.

The performance of both WaveNet and the EDD models was extensively optimized before we applied the resampling strategies: the goal of this paper is to use data imbalance strategies to improve an already peak performing scheme. This included the consideration of different loss functions during training and regularization

**Table 1**  
Number of Trainable Parameters in Section of Each Model Architecture

Model type/size	Convolutional layers	Dense layers	Number of layers per section
Small EDD	26,237	328,800	3/3
Large EDD	50,337	650,800	3/3
Model type/size	Shared layers	Branched layers	Number of layers per section
Small WaveNet	10,368	342,177	1/3
Large WaveNet	14,904	704,385	1/3

*Note.* The EDD is comprised of three sections: encoder, dense, decoder; WaveNet is comprised of two sections: shared layers and 33 branches for the top 33 pressure levels.

to avoid overfitting. The schemes were regularized by applying both L1 and L2 regularization to encourage sparsity as well as weight decay. The L1 and L2 regularization coefficients were tuned during our initial hyperparameter tuning step using RayTune (Liaw et al., 2018). We observed significant gaps in performance between training and validation test sets with too little regularization. With too much regularization, however, overall performance began to suffer in both the training and validation sets such that most predictions were being damped to predicting zero profiles. RayTune enabled us to do a systematic search for optimal regularization parameters in a simple and efficient way.

The absolute norm error of a  $p$ -length profile is proportional to the root mean squared error,

$$AE(y, \hat{y}) = \|y - \hat{y}\|_2 = \left( \sum_{j=1}^p (y[j] - \hat{y}[j])^2 \right)^{1/2} = \sqrt{p} \text{RMSE}(y, \hat{y}),$$

and was shown, for instance in Figure 2. To better assess the skill of the data-driven parameterizations, we normalize the absolute error by the RMS amplitude of the target GW drag predictions. For a set of  $N$  target profiles  $\{y_i\}_{i=1}^N$  and their corresponding prediction profiles  $\{\hat{y}_i\}_{i=1}^N$ , the relative is computed as

$$RE(\{y_i\}_i, \{\hat{y}_i\}_i) = \frac{\sum_i AE(y_i, \hat{y}_i)}{\sum_i \|y_i\|_2}.$$

A relative norm error of 1 (100% error) would imply that the average magnitude of the error is as large as the average magnitude of the target profiles: a scheme predicting zero drag for all profiles in this wind range bin would satisfy this condition. Furthermore, the RE ensures that the trend of the error norms over the wind range is not simply proportional to the trend of the target vector norms.

Figure 5 shows the absolute and relative errors of the four models with no resampling strategy, establishing a baseline for comparison with our resampling strategies. We have omitted analysis of the bins where the zonal wind range is less than 5 m/s or greater than 200 m/s, corresponding to 0.0085% and 0.00055% of the data set, respectively. With so few data points, the errors in these bins are noisy and dominated by sampling error. We show the relative error on the right panel to highlight how all four variants learn the peak portion of the distribution best, but struggle with both tails.

We emphasize that relative errors are normalized separately for each bin of the zonal wind range. While the absolute errors are small for low wind range cases, the target GW tendencies are also small, so that the scheme is not doing so well relative to a straightforward climatological prediction, particularly with the WaveNet models. A key region in need of improvement, however, is where wind range is greater than 175 m/s. Here both the absolute and relative errors in all 4 schemes are large.

We observe that the EDD models outperform the WaveNet models, and this disparity in errors between the model architectures is more significant than between network sizes. The relative error is below 30% for a wind range of approximately 45–175 m/s for two WaveNet models, and for a larger range for EDD, 25–175 m/s. Despite having approximately the same number of learnable parameters as their EDD counterparts, the WaveNet models have not

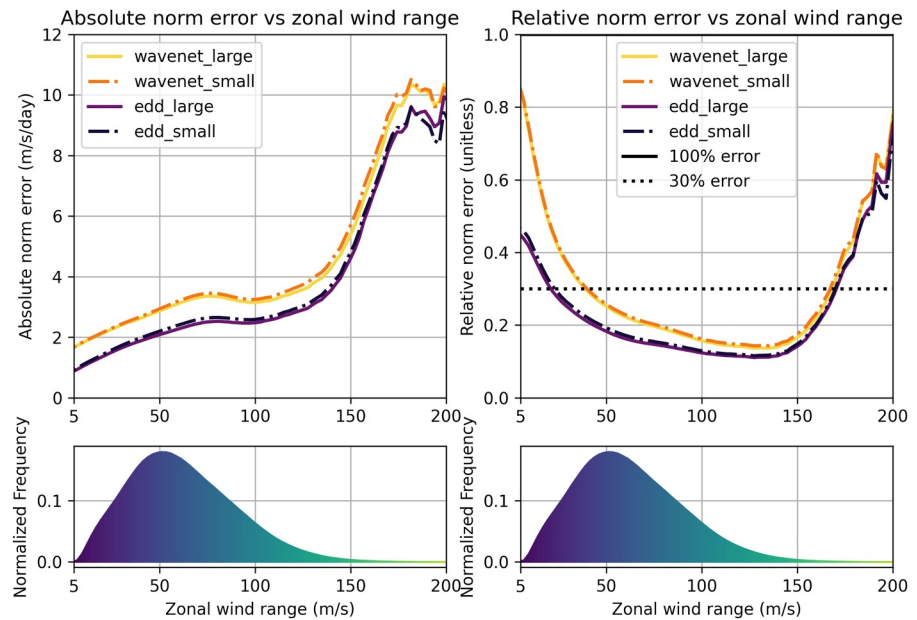


**Figure 5.** Baseline ( $t = 0$ ) absolute and relative error norms of two sizes of WaveNet and EDD are shown. The errors are shown as a function of wind range in the validation set, as in Figure 2, which showed results only from the large WaveNet model.

acquired as much skill given identical training conditions; the number of learnable parameters alone cannot fully quantify model complexity.

#### 4.2. Data Resampling and Offline Results

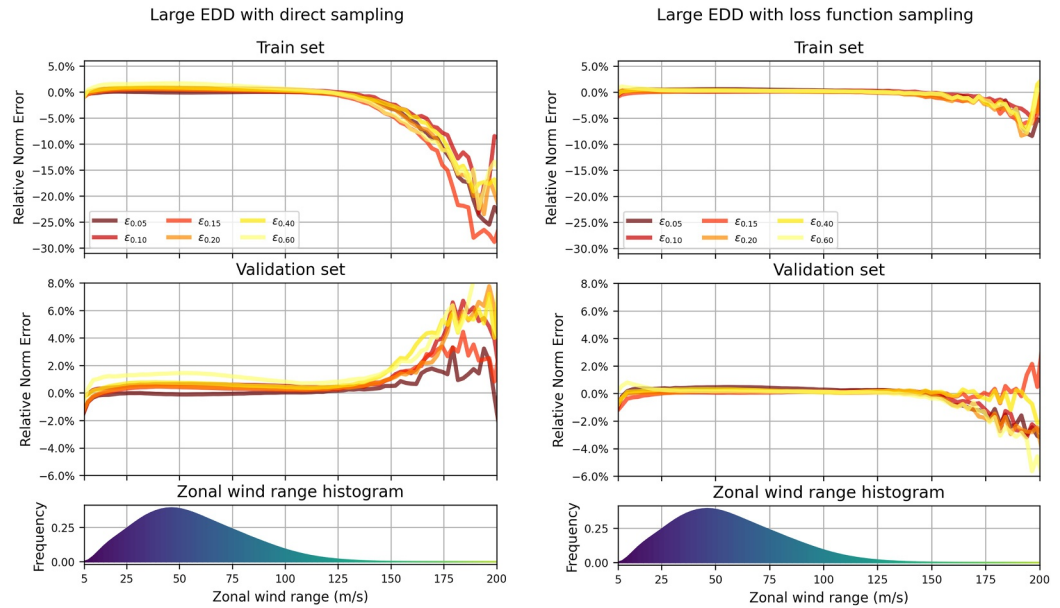
Of the three tunable parameters of the resampling strategy, we focus primarily on the impact of  $t$ , after a brief discussion of the maximum repeat parameter in Section 3.2.3. The resolution of the histogram was set at 100 equal-width bins after an initial survey. We investigated values of  $t = 0.05, 0.10, 0.15, 0.20, 0.40, 0.60$  following intuition that  $t$  closer to 1 is likely more damaging than helpful given the shape of the distribution of our data set. Figure 4 shows the new shape of the data distribution of the 6 configurations on the teal (medium-width) lines with the original distribution shaded in green in the background.

Figures 6–9 show the baseline error ( $t = 0$ , shown in Figure 5) in black lines, and the deviation of the error relative to this baseline for  $t > 0$  in colors ranging from brown to yellow. In all instances we see very little, if any, loss of accuracy in the peak region (a wind range of roughly 10–100 m/s). We have achieved one criterion for success: resampling, either directly or through a weighted loss function, does not damage performance for typical inputs. Now the harder part: does resampling improve performance in the tail, from 100 to 200 m/s in our wind range metric? Here we found success in most cases, though not uniformly. We acknowledge the failure first. In our best baseline network, the large EDD, direct oversampling led to overfitting. In all other cases, however, we were able to successfully reduce error in the tail.

##### 4.2.1. Maximum Repeat

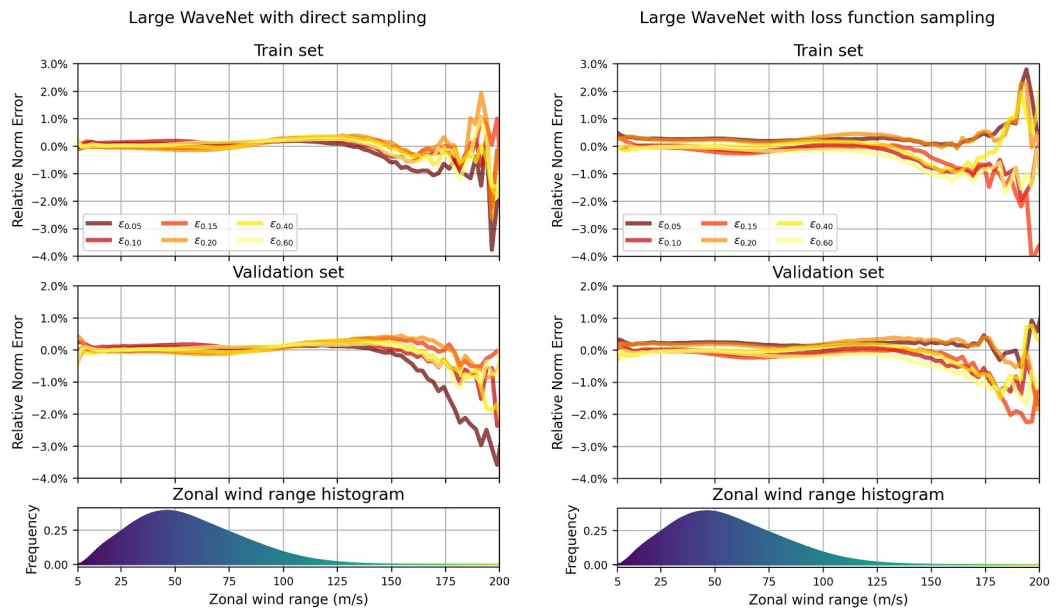
The `max_repeat` parameter sets a ceiling on the value of  $\alpha$  to prevent overfitting in the extreme tail and should be calibrated based on the distribution of the data set and renormalization  $t$  value. In our application, adjusting `max_repeat` allowed us to draw more attention to samples with a wind range from 100 to 200 m/s while avoiding too much attention to the extreme values with a wind range beyond 200 m/s, where there were insufficient samples for robust learning.

Figure 4 shows the effect of `max_repeat` on sampling profiles with zonal wind range from 100 to 200 m/s versus above 200 m/s. When `max_repeat = 10` (black line in Figure 4), oversampling of profiles with a wind range between 100 and 200 m/s is curtailed for all values of  $t$ ; for  $t = 0.6$ , throttling begins with a wind range of



**Figure 6.** This figure shows the results of applying data rebalancing to the large EDD model architecture with the direct sampling method (left column) and the loss function sampling method (right column). The plotted error function,  $\epsilon_t(n)$ , is the difference in the relative norm error of a model trained with a positive  $t$ -value to the model trained without any data rebalancing ( $t = 0$ ) in the  $n$ th bin, where negative values indicate improvement. The colors brighten as  $t$  increases, and the reference baseline error is shown in Figure 5. The top and middle rows show the error differences on the training and validation sets, and the bottom row shows the histogram of the data set with respect to the zonal wind range between 5 and 200 m/s.

approximately 150 m/s. This limits attention on profiles that we care about. When `max_repeat` is set to 100 (green line), throttling begins at a zonal wind range greater than 200 m/s for  $t = 0.05, 0.10,$  and  $0.15,$  and for `max_repeat` = 500 (yellow line), the cap on  $\alpha$  only affects the sampling of profiles with a wind range greater than 200 m/s for all  $t$  values. Further increasing `max_repeat` will thus have no impact on our range of interest.



**Figure 7.** Both columns show errors in the same fashion as Figure 6. Left column shows errors for the large WaveNet instances with direct sampling implementation, and right column shows errors for the large WaveNet instances with weighted loss function sampling implementation.

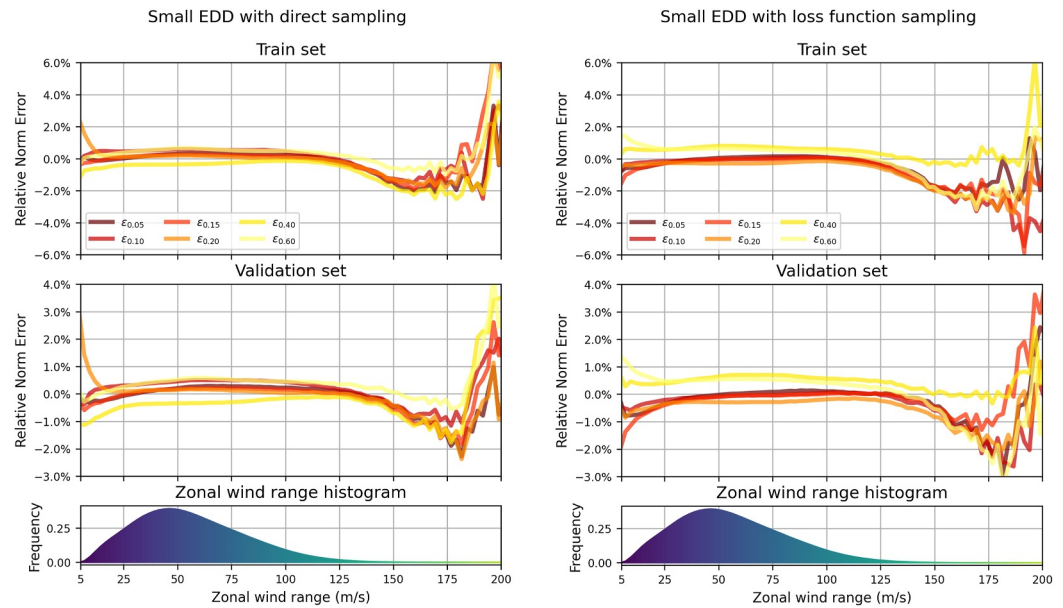


**Figure 8.** Both columns show errors in the same fashion as Figure 6. Left column shows errors for the small EDD instances with direct sampling implementation, and right column shows errors for the small EDD instances with weighted loss function sampling implementation.

There is a cost, however, to setting `max_repeat` too high. Once the “moderate” tail that we care about saturates, further oversampling only draws more attention to the most extreme values. To quantify this effect, we show the proportion of the rebalanced data set that corresponds to samples with zonal wind range between 100 and 200 m/s and greater than 200 m/s in Table 2. In the original data set, 12.43% and 0.0065% of samples are found in these two ranges, respectively. For small values of `max_repeat`, increasing  $t$  leads to a dramatic increase in the percentage of samples with a wind range of 100–200 m/s, without substantially increasing the focus on profiles >200 m/s. As `max_repeat` increases, however, more focus shifts to the extreme tail, and the percentage of

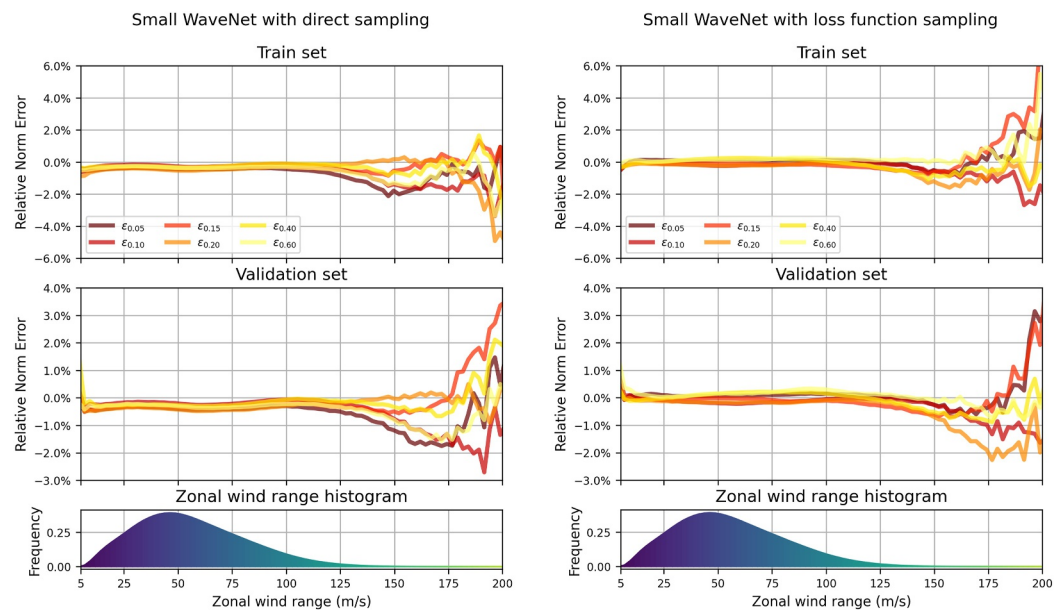


**Figure 9.** Both columns show errors in the same fashion as Figures 6–8. Left column shows errors for the small WaveNet instances with direct sampling implementation, and right column shows errors for the small WaveNet instances with weighted loss function sampling implementation.

**Table 2**  
Percentage of the Rebalanced Data Set Corresponding to Samples With Zonal Wind Range 100–200 m/s (First Number) Versus Greater Than 200 m/s (Second Number) as Set by Combinations of  $t$  and  $\text{max\_repeat}$  Values

		max_repeat		
		10	100	500
The box adjacent to max_repeat and 10 cells				
$t$	0.05	14.00/0.07	14.06/0.43	14.02/0.66
	0.10	15.36/0.07	15.73/0.62	15.66/1.09
	0.15	16.60/0.07	17.45/0.67	17.30/1.49
	0.20	17.78/0.07	19.17/0.67	18.97/1.83
	0.40	22.36/0.07	26.02/0.70	25.89/2.89
	0.60	27.20/0.08	33.02/0.73	33.29/3.45

samples with a wind range of 100–200 m/s starts to drop as a growing fraction of the rebalanced data set is in the extreme tail.

For a given value of the rebalancing parameter  $t$ , the proportion of samples in the moderate tail reaches a maximum at a different value of  $\text{max\_repeat}$ . For simplicity, we fixed  $\text{max\_repeat}$  at 100 for all our experiments, as it was near this optimum for most of the  $t$  values. A slightly lower value would be optimal for the small  $t$  value cases, while  $\text{max\_repeat} = 500$  would be more optimal for  $t = 0.6$ , but we found that the effect was small.

#### 4.2.2. Overfitting Versus Underfitting

As we feared, the resampling strategy can encourage overfitting of the tail in a data-driven scheme with sufficient complexity. Figure 6 shows the result of training the large EDD model. The left panel shows the direct sampling implementation (Algorithm 2). For the direct sampling implementation, samples with wind range greater than 125 m/s in the training set suggest

impressive gains when compared to the baseline error, albeit with no clear correlation with the  $t$  parameter. This improvement, however, fails to generalize to samples unseen during training: the mean absolute error of the validation set is larger than that of the baseline error. We observe that larger  $t$  corresponds to larger growth in error, suggesting that the trained models suffer from overfitting triggered by the inflation of samples in the moderate tail region.

Typically, overfitting is diagnosed during training when validation error stops improving (or even start to get worse) while training error further improves. We avoided overfitting for the baseline WaveNet and EDD by applying L1 and L2 regularizations during training. While we only show the errors at the end of training, it is clear from the design of this experiment that the resampling strategy resulted in models that learned the noise at the tail rather than learning an intrinsic principle tied to the tail. A potential cause for overfitting is larger model complexity (number of trainable parameters) relative to the complexity of the pattern being learned, which then leads to the model learning noise associated with the specific instance of the training set. We suspect that oversampling of the tail combined with the large network size created a learning environment in which the EDD had the capacity to learn noise in the tail. It might be possible to mitigate this overfitting by increasing the regularization of the EDD. When training without resampling, however, we found that increased regularization was starting to reduce overall performance.

The right panel of Figure 6 shows the experiment results with the weighted loss implementation (Algorithm 3). Note that Figures 6–9 all show the error deviation from the baseline, where negative values indicate improvement. Unlike the direct sampling implementation, we observe about the same magnitude of improvement in the tail for the training set and the validation set. The upper-middle range  $t$ -values (0.15, 0.20, 0.40) exhibit no improvements from the baseline in the validation set, but the extreme  $t$ -values (0.05, 0.10, 0.60) all show slight improvements. Since the only difference between the left and the right panels is in the implementation details of the resampling strategy, this suggests that the weighted loss function implementation may be less amenable to overfitting than the direct sampling method. We further analyze the comparison between the two implementation methods in Section 4.2.3.

Next, we repeat the experiment in the previous section for the large WaveNet architecture, which has a comparable number of tunable parameters for both implementation methods, and show the result in Figure 7. We observe that the validation set errors at the tail are smaller than the baseline error for most  $t$  values, and there is no significant change to the errors at the peak. Unlike the example in Figure 6, these large networks did not overfit to the samples at the tail of the training set relative to the baseline error. If network size is a potential cause for overfitting in the direct sampling large EDD case, why do we not see similar results in the large WaveNet cases?

We speculate that the baseline WaveNet model was underfitting and there was more room for improvement to be garnered from applying the resampling strategy. If the baseline EDD model was not underfitting, then the resampling strategy could not reduce the approximation error (bias) much more than was already achieved by the baseline model, and all there was left to learn were noisy traits unique to the training set.

With the exception of the overfitting case, the resampling strategy successfully reduces underfitting at the tail without penalty in the peak, thereby reducing the bias overall. In the next section, we show further evidence of success of the resampling strategy and compare the two implementation methods.

#### 4.2.3. Sampling Strategy Comparison: Weighted Sampling Versus Weighted Loss

We now compare the two implementations (Algorithms 2 and 3) on the small EDD models. Figure 8 shows the baseline errors and the deviations from the baseline errors as we vary  $t$  over the training and the validation sets. Figure 8 reveals improvements in the tail, albeit modest, with little to no loss in accuracy in the peak. The notable exceptions occur at  $t = 0.20$  and  $t = 0.40$  for the weighted loss implementation, where there are almost no change if not a decline in performance on the tail. These occur in both the training and validation set, however, and therefore are not likely an issue of overfitting. Outside of those exceptions, improvements occur for a wider range of the distribution, with larger magnitudes of improvement in the training set than in the validation set as expected. The weighted loss experiment (right plots of Figure 8) shows a slightly larger disparity between the training and validation set errors than the direct sampling experiment; the training set errors show larger improvements with the weighted loss implementation than direct sampling, but the validation errors are comparable between the two implementations. With direct sampling, all  $t$  values except for  $t = 0.60$  still yield improvement in error in the moderate tail region.

Next, we discuss the experiment results for the small WaveNet model. As shown in Figure 9, the difference between direct sampling and weighted loss are less pronounced than in the EDD model. Also, the errors of the training set and the validation set are much closer than in the experiments for the small EDD models. The largest difference between the implementation methods for the small WaveNet models is in which  $t$  values are the most optimal. The direct sampling method is optimized for the smallest and largest  $t$  values, whereas the weighted loss method prefers moderate  $t$  values ( $t \approx 0.15$ ).

Even though we saw that the loss function sampling avoided overfitting for the large EDD experiment, we do not see a similar advantage of the loss function implementation over the direct sampling implementation in the small EDD, small WaveNet, and large WaveNet experiments. However, we do see modest improvements in the tail for models trained with the resampling strategy for the majority of  $t$  values for those three experiments, although there is no clear trend of which  $t$  values are optimal. Future experiments that may reveal tighter trends, include studying the sensitivity of learning algorithm, and increasing the density of  $t$  values.

### 4.3. Bias Removal and Online Results

We conclude our case study with a brief discussion of how our modified data-driven parameterizations perform when coupled “online” with the MiMA atmospheric model. An important evaluation of a new parameterization scheme is conducted by computing statistics from long-time integrations where the scheme is coupled with the model, as opposed to the “offline” metrics we showed in the previous section. Online coupling is a more challenging task, as errors in the GWP can lead to biases in the large scale flow, forcing the scheme to make inferences in regimes it has not yet seen, which often leads to instability (Brenowitz et al., 2020).

To test a selection of our trained ML emulators, we follow Espinosa et al. (2022), coupling them with MiMA for 40-year integrations after 20 years of model spin-up. The simulations with the data-driven emulators can then be compared against the control integration with the “true” GW forcing provided by the AD99 physics-based parameterization. Coupling also allowed us to implement the bias correction, which can be implemented independently or in addition to the rebalancing strategies. To summarize quickly, the new data-driven parameterizations successfully couple with the model, producing climatological statistics (mean and variability) that were consistent with the original model. Differences between the model with the baseline schemes and our re-balanced versions, however were not statistically significant. It is likely that a longer integration could eventually reveal significant differences, but an improvement that requires a century or more to observe is of modest utility. We conclude that while re-balancing the data did improve performance based on the wind range metric, this bias was either not critical to performance of the parameterization in the model, or we have not sufficiently improved the tails to see a significant effect.

For completeness, we show a few results here, focusing on the coupled model's ability to generate the Quasi-Biennial Oscillation (QBO), a vacillation of easterly and westerly jets in the tropical stratosphere over a

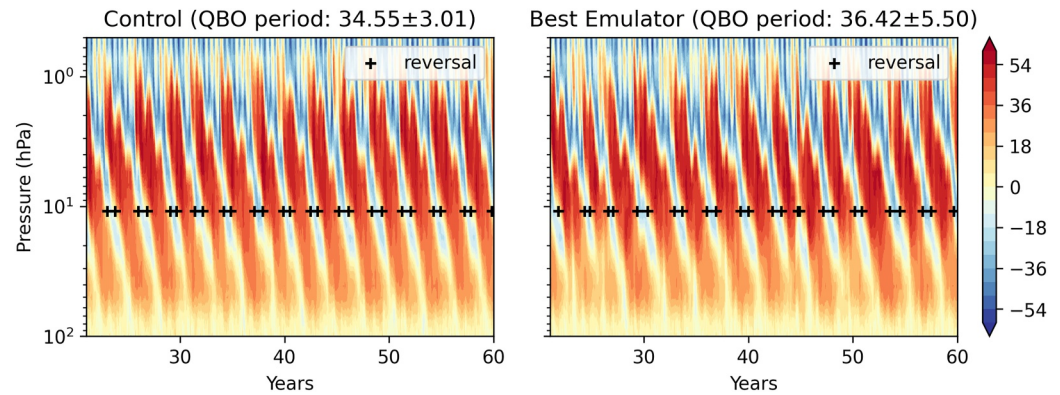


**Figure 10.** Both plots show the zonal mean zonal wind averaged over years 20–40 in latitudes between 5°S and 5°N. The crosses indicate the times where Quasi-Biennial Oscillation phase changes are detected by the Transition Time method. Left: Control run with AD99; Right: Best emulator (small EDD with resampling strategy via weighted loss and  $t = 0.05$  and bias removal).

period of approximately 28 months. We highlight this metric because the QBO is in large part driven by GW momentum transport. This emergent behavior on a time scale of years, generated from gravity waves that operate on time scales of hours, is viewed as critical test of GW parameterizations (Anstey et al., 2022; Bushell et al., 2022; Richter et al., 2022). An important difference between the online runs in this manuscript and that of Espinosa et al. (2022) is in the model parameters of MiMA that generated the training data. We employed parameters that were optimized for simulation of the Northern hemisphere (Garfinkel et al., 2020), not the QBO. Thus the oscillation in the control integration had a period of approximately 35 months, not 28 months, as shown in Figure 10. Capturing the right period of the QBO is generally achieved by tuning the GWP, as was done in Garfinkel et al. (2022).

We show results with the smaller EDD models, as the rebalancing strategies exhibited the largest offline improvement. Table 3 lists the QBO period for the baseline model ( $t = 0$ ) and the various combination of resampling strategy and bias removal. The QBO period was computed using the Transition Time (TT) method of Richter et al. (2020). First, the zonal wind was averaged zonally in the tropical region (latitudes between 5°S and 5°N), as shown in Figure 10. Then the intervals between QBO phase changes are defined as times when the signs of zonal mean zonal wind reversal near 10 hPa (denoted by the plus signs). The resulting mean and the standard error of those values give us a proxy for a confidence interval of the QBO period. A robust implementation of the TT method requires smoothing the field with 15–30 days windows, to avoid double counting small deviations around transitions.

The baseline model exhibited a slightly longer QBO period of 38 months, though 40 years of simulation was insufficient to establish whether this bias is statistically significant. We found that all of our modified data-driven approaches exhibited shorter QBO periods, an improvement relative to the baseline, but still biased long relative to the control. The best performing model is highlighted in Figure 10, but as quantified in Table 3, these integrations are not long enough to establish whether these differences are statistically significant. As noted above, this could be due to the fact that the QBO bias is unrelated to errors in the rare cases highlighted by the wind range metric, or that our correction is insufficiently large to make a dent. It highlights the importance of domain knowledge to identify the key quantity or quantities of data imbalance that matter for the problem of interest.

**Table 3**  
*Means and Standard Errors of the Quasi-Biennial Oscillation Periods Computed With the Transition Time Method for Various Machine Learning Emulators Coupled to MiMA*

Emulator description	Transition time
Control	$35.0 \pm 2.5$
Small EDD, $t = 0$	$38.4 \pm 6.6$
Small EDD, $t = 0$ , bias removed	$37.0 \pm 7.7$
Small EDD, $t = 0.05$ , direct sampling	$37.0 \pm 3.0$
Small EDD, $t = 0.05$ , direct sampling, bias removed	$38.1 \pm 3.7$
Small EDD, $t = 0.05$ , weighted loss	$39.7 \pm 9.0$
Small EDD, $t = 0.05$ , weighted loss, bias removed	$36.4 \pm 5.5$

## 5. Conclusions and Future Directions

With the growing prevalence data-driven methods being used for various tasks in modeling earth system models, it is crucial to properly learn from geoscience data sets. We address what one can do to improve a data-driven parameterization given that there is no additional data to learn from, nor

computational capacity to allow for a larger, more complex model. In other words, this is the typical scenario for modeling various subgrid-scale mechanisms in climate models. In particular, we proposed two strategies to combat data imbalance with the goal of improving data-driven models, and applied it to a case study of improving a data-driven GWP model.

Both methods rely on first identifying a metric or a projection that yields reveal an imbalance in the available data set that has an inherent significance to the physical process being modeled. This process is unique to each application and requires expert scientific knowledge of the modeled process, and doubles as a dimension reduction step that allows the practitioners to view the original high-dimensional data set in a new context. Ideally, this new context should illuminate the differences between frequent (and therefore easy to model) instances from rare (and difficult to model) instances. Despite resulting from the same physical mechanisms, these two types of instances occupy almost two distinct regimes due to the natural variability in the model system. A necessary complicating factor is that these two *classes* are not sharply partitioned like discrete distributions, but rather can be viewed as the peak and the tail of a continuous distribution. In our case study, we chose wind range of a model column as the appropriate metric for our physical process, gravity waves. This choice stemmed from the observation that wind range can crudely approximate shear, an important quantity in determining the level at which GWs break.

Data rebalancing can be achieved in two ways. In the first method, we use the distribution of the data set along the identified metric to systematically undersample from the peak and oversample from the tail. Our motivation to undersample from the peak is from the intuition that these samples are over-represented relative to the variability they cover within the data set, resulting in trained models that may overfit to this region. On the other hand, oversampling the tail is justified by the exact inverse logic: these rare samples are undervalued in their influence over training models. In the second method, the sampling is left unchanged, but the loss function is weighted by the same ratio to increase the penalty on the under-represented class and reduce it for over-represented class. Both data rebalancing strategies generate a new distribution/weighting function on the training data set with a linear interpolation of the original distribution to a desired distribution (i.e., uniform distribution) parameterized by  $t \in [0, 1]$ , much like histogram equalization. We add in an additional parameter to prevent too much oversampling/weighting in the tail, by the name of maximum repeat. The implementation of these methods requires discretizing the continuous distribution into discrete bins; the choice of the histogram is also an important choice. The methods are implemented by either providing to the learning algorithm a subsample of the data set that realizes the new distribution, or using the new weights in the loss function such that the new distribution is implicitly represented.

In our case study, we found that data rebalancing can successfully reduce the errors in the moderate tail region while maintaining approximately the same error levels in the peak under most scenarios. Success depended on the complexity of the model, and data resampling increased the generalization error in the tail with our most complex models. Too much complexity can allow a model to learn noise rather than pattern in the data set, a phenomenon exacerbated by oversampling in the tail. We do not observe a clear advantage of the direct sampling implementation over the weighted loss implementation in the efficacy of the rebalancing method, nor an unambiguous indication of how to choose the method parameters. The rebalancing parameter  $t$  controls the degree to which the data set is leveled, the number of histograms controls the granularity of the redistribution, and the maximum repeat parameter allows one to limit focus on the extreme ends of the distribution.

When considering the ease of use between the two implementations, we expect that the weighted loss method would be preferable when working with large data sets, and for most commonly used loss functions. Loss functions that cannot be easily decomposed for sample-wise evaluations do exist (i.e., some sequence, ranking, kernel and distribution-based losses) but most are compatible and therefore this issue may be of small concern for most applications. The direct sampling method requires potentially reshaping the data array, which can be memory intensive for very large data sets. Although this can be minimized by applying the rebalanced sampling to smaller batches of data, this then restricts some choices of the optimization hyperparameters which may be suboptimal. For smaller data where this is not an issue, the direct sampling method can be preferable since it does not impact the algorithm part of the training process, which may allow for a greater freedom in exploring the algorithmic space.

Mean bias removal, an additional approach to fix errors with data imbalance, corrects the extant bias in a fully trained data-driven model as a function of the data imbalance-revealing metric This is a first-order correction as it

assumes that the mean bias profile of the trained model evolves meaningfully across this metric. The main source of error for this method is generalization error as the mean bias profiles of the training set may not be representative of the instances available at time of inference.

In conclusion, data rebalancing and bias removal show modest improvements in producing data-driven models less inclined to mirror the imbalance apparent in the data set. We attribute the lack of overwhelming evidence of the success of these methods to two main factors. The first was the projection used to identify data imbalance, a crucial component to both data rebalancing and mean bias removal. We used a baseline NN emulator of AD99 to diagnose coordinates along which heteroscedastic error persisted. Conspicuous coordinates such as latitude, longitude, and time-of-year yielded uniform errors, and feature important analysis pointed towards uncertainty associated with shear in the wind profiles. We found the wind range metric to be the most promising direction out of the potential metrics we explored, but it still may not be the most ideal projection for the data set used in our case study. It is also possible that any 1D projection is too simple to capture the data imbalance for this data set. The rebalancing strategy can be extended to higher dimensions, although the data requirements will grow rapidly.

Second, our assumptions on how the data imbalance impacts the training of the data-driven models may be overly simplistic, especially in its treatment of the tail. We view samples from the tail as in need of a greater significance in training the ML model. However, a more pressing issue at the tail may be that the data set available to us does not cover the variability inherent to that region. If so, any oversampling does not increase coverage in this region but instead lead to overfitting. We attempt to curb this by introducing the maximum repeat parameter, but this introduces another parameter to be tuned in the rebalancing method. Scarcity of rare (and extreme) phenomena in data sets is a common challenge in geoscience data sets that may be alleviated by rare event sampling strategies.

## Appendix A: Formal Algorithm Details

Algorithm 1 shows an example of how to incorporate the direct sampling implementation of the resampling strategy within the framework of any stochastic gradient descent-type learning algorithm that processes batches of training samples at a time. Next, Algorithms 2 and 3 show the direct sampling and weighted loss sampling implementations in detail. Algorithm 1 can easily be modified to use Algorithm 3, where the computed weights are passed into the loss function in the optimization step in line 6, and lines 1, 3, and 4 can be omitted.

---

**Algorithm 1** : Training structure.

---

**Input:**  $\mathcal{X}$ , Training set;  $\hat{\phi}$ , machine learning model;  $\{C_n^{(1)}\}_{n=1}^N$ , counts of bins of ideal histogram;  $t$ , linear parameter; **max\_repeat**, maximum repeat parameter.

- 1  $\{I_n^{(0)}\}_{n=1}^N \leftarrow$  Bin  $\mathcal{X}$  into  $N$  bins.      //  $I_n^{(0)}$  is the list of indices in the  $n$ th bin.
- 2 **while**  $\hat{\phi}$  needs further improvement **do**
  - 3     // This while-block encompasses a pass over the training set.
  - 3      $I^{(t)} \leftarrow$  resample( $\{I_n^{(0)}\}_{n=1}^N, \{C_n^{(0)}\}_{n=1}^N, t, \text{max\_repeat}$ )
  - 4     Shuffle  $I^{(t)}$  and divide it into  $B$  batches ( $I^{(t)} = \cup_{b=1}^B I_b$ ).
  - 5     **for**  $b=1:B$  **do**
  - 6         | Optimize  $\hat{\phi}$  over  $\mathcal{X}[I_b]$ .
- 7 **return**  $\hat{\phi}$       // Trained model

---

---

**Algorithm 2 :**  $I^{(t)} \leftarrow \text{resample}(\{I_n^{(0)}\}_{n=1}^N, \{C_n^{(1)}\}_{n=1}^N, t)$ .

---

**Input:**  $\{I_n^{(0)}\}_{n=1}^N$ , binned indices;  $\{C_n^{(1)}\}_{n=1}^N$ , counts of bins of ideal histogram;  $t$ , linear parameter; `max_repeat`, maximum repeat parameter.

//  $I_n^{(0)}$  is the list of indices in the  $n$ th bin.

```

1  $I^{(t)} \leftarrow []$  //  $I^{(t)}$  is an empty list.
2 for  $n = 1 : N$  do
3   Compute  $\alpha_n^{(t)}$ . // Use Eqs. (3) to (5).
4    $l \leftarrow c_n^{(t)}$ 
5   if  $\alpha_n^{(t)} \geq 1$  then
6     Append  $I_n^{(0)}$   $\text{floor}(\alpha_n^{(t)})$  times to  $I^{(t)}$ .
7      $l \leftarrow c_n^{(t)} - (\text{count}(I_n^{(0)}) \times \text{floor}(\alpha_n^{(t)}))$ .
8     //  $l$  is now an integer that satisfies  $0 \leq l \leq \text{count}(I_n^{(0)})$ .
9     Append a random subset of  $I_n^{(0)}$  with length  $l$  picked without replacement to  $I^{(t)}$ .
9 return  $I^{(t)}$  // New indices.
```

---



---

**Algorithm 3 :**  $J \leftarrow \text{weights}(\{I_n^{(0)}\}_{n=1}^N, \{C_n^{(0)}\}_{n=1}^N, t, M)$ .

---

**Input:**  $\{I_n^{(0)}\}_{n=1}^N$ , binned indices;  $\{C_n^{(1)}\}_{n=1}^N$ , counts of bins of ideal histogram;  $t$ , linear parameter;  $M$ , the size of dataset.

//  $I_n^{(0)}$  is the list of indices in the  $n$ th bin.

```

1  $J \leftarrow \text{zeros}(M)$  //  $I^{(t)}$  is an empty list.
2 for  $n = 1 : N$  do
3   Compute  $\alpha_n^{(t)}$ . // Use Eqs. (3) and (4).
4    $J[I_n^{(t)}] = \alpha_n^{(t)}$ 
5 return  $J$  // New weights for samples.
```

---

## Appendix B: Architecture Details

We process each of the input features separately with the 1D convolutions. To achieve this, we horizontally stack the features (vertical profiles of zonal wind,  $U$ , meridional wind,  $V$ , vertical wind,  $\omega$ , temperature,  $T$  as “channels”), resulting in a 2D input shape of `nlev`  $\times$  4. (Note that the nomenclature of channels originates from Red Green Blue (RGB) channels in image processing.) Additional information such as longitude, latitude, and surface pressure are concatenated to the flattened output of the encoder. The resulting 1D array is pushed through dense layers intended to represent global relations. Finally, the output from the dense section is reshaped to be processed via transposed convolutions and upsampling layers in the decoder.

## Conflict of Interest

The authors declare no conflicts of interest relevant to this study.

## Data Availability Statement

All neural networks used in this manuscript were (re-)written in PyTorch (Paszke et al., 2019). The WaveNet implementation in PyTorch exactly followed the descriptions in Espinosa et al. (2022). Model of an Idealized Moist Atmosphere (MiMA) (Garfinkel et al., 2020; Jucker & Gerber, 2017) is available and maintained at (Jucker et al., 2020) and <https://github.com/mjucker/MiMA>. The model code, forpy coupling code, trained NNs, run

parameters, and modified configuration for MiMA are available at <https://doi.org/10.5281/zenodo.18451774> (Yang, 2026). The coupling library, forpy, developed and maintained by Elias Rabel is well documented and available at <https://github.com/ylikx/forpy> (Rabel et al., 2018).

### Acknowledgments

This work was supported by the U.S. National Science Foundation through award OAC-2004572 and Schmidt Sciences, as part of the Virtual Earth System Research Institute (VESRI). The manuscript benefited greatly from conversations with Joan Alexander and Pedram Hassanzadeh, and from constructive comments on an earlier version of the manuscript from two anonymous reviewers. We also thank the NYU High Performance Computing center, where the model integrations were performed.

### References

- Alexander, M. J., & Dunkerton, T. J. (1999). A spectral parameterization of mean-flow forcing due to breaking gravity waves. *Journal of the Atmospheric Sciences*, *56*(24), 4167–4182. [https://doi.org/10.1175/1520-0469\(1999\)056<4167:ASPOMF>2.0.CO;2](https://doi.org/10.1175/1520-0469(1999)056<4167:ASPOMF>2.0.CO;2)
- Anstey, J. A., Osprey, S. M., Alexander, J., Baldwin, M. P., Butchart, N., Gray, L., et al. (2022). Impacts, processes and projections of the quasi-biennial oscillation. *Nature Reviews Earth & Environment*, *3*(9), 588–603. <https://doi.org/10.1038/s43017-022-00323-7>
- Brenowitz, N. D., Beucler, T., Pritchard, M., & Bretherton, C. S. (2020). Interpreting and stabilizing machine-learning parametrizations of convection. *Journal of the Atmospheric Sciences*, *77*(12), 4357–4375. <https://doi.org/10.1175/jas-d-20-0082.1>
- Brenowitz, N. D., & Bretherton, C. S. (2019). Spatially extended tests of a neural network parametrization trained by coarse-graining. *Journal of Advances in Modeling Earth Systems*, *11*(8), 2728–2744. <https://doi.org/10.1029/2019MS001711>
- Bushell, A., Anstey, J., Butchart, N., Kawatani, Y., Osprey, S., Richter, J., et al. (2022). Evaluation of the quasi-biennial oscillation in global climate models for the SPARC QBO-Initiative. *Quarterly Journal of the Royal Meteorological Society*, *148*(744), 1459–1489. <https://doi.org/10.1002/qj.3765>
- Chanry, M., Hatfield, S., Dueben, P., Polichtchouk, I., & Palmer, T. (2021). Machine learning emulation of gravity wave drag in numerical weather forecasting. *Journal of Advances in Modeling Earth Systems*, *13*(7), e2021MS002477. <https://doi.org/10.1029/2021MS002477>
- Chawla, N. V., Bowyer, K. W., Hall, L. O., & Kegelmeyer, W. P. (2002). SMOTE: Synthetic minority over-sampling technique. *Journal of Artificial Intelligence Research*, *16*, 321–357. <https://doi.org/10.1613/jair.953>
- Chawla, N. V., Japkowicz, N., & Kotcz, A. (2004). Special issue on learning from imbalanced data sets. *ACM SIGKDD Explorations Newsletter*, *6*(1), 1–6.
- Connelly, D. S., & Gerber, E. P. (2024). Regression forest approaches to gravity wave parameterization for climate projection. *Journal of Advances in Modeling Earth Systems*, *16*(7), e2023MS004184. <https://doi.org/10.1029/2023MS004184>
- Ding, D., Zhang, M., Pan, X., Yang, M., & He, X. (2019). Modeling extreme events in time series prediction. In *Proceedings of the 25th ACM SIGKDD International Conference on Knowledge Discovery & Data Mining* (pp. 1114–1122). ACM. <https://doi.org/10.1145/3292500.3330896>
- Elkan, C. (2001). The foundations of cost-sensitive learning. In *International Joint Conference on Artificial Intelligence* (Vol. 17, pp. 973–978). Lawrence Erlbaum Associates Ltd.
- Espinosa, Z. I., Sheshadri, A., Cain, G. R., Gerber, E. P., & DallaSanta, K. J. (2022). Machine learning gravity wave parameterization generalizes to capture the QBO and response to increased CO<sub>2</sub> [Software]. *Geophysical Research Letters*, *49*(8), e2022GL098174. <https://doi.org/10.1029/2022GL098174>
- Garfinkel, C. I., Gerber, E. P., Shamir, O., Rao, J., Jucker, M., White, I., & Paldor, N. (2022). A QBO cookbook: Sensitivity of the quasi-biennial oscillation to resolution, resolved waves, and parameterized gravity waves. *Journal of Advances in Modeling Earth Systems*, *14*(3), e2021MS002568. <https://doi.org/10.1029/2021ms002568>
- Garfinkel, C. I., White, I., Gerber, E. P., Jucker, M., & Erez, M. (2020). The building blocks of Northern Hemisphere wintertime stationary waves. *Journal of Climate*, *33*(13), 5611–5633. <https://doi.org/10.1175/jcli-d-19-0181.1>
- He, H., & Garcia, E. A. (2009). Learning from imbalanced data. *IEEE Transactions on Knowledge and Data Engineering*, *21*(9), 1263–1284. <https://doi.org/10.1109/TKDE.2008.239>
- Johnson, J. M., & Khoshgoftaar, T. M. (2019). Survey on deep learning with class imbalance. *Journal of Big Data*, *6*(1), 27. <https://doi.org/10.1186/s40537-019-0192-5>
- Jucker, M., & Gerber, E. P. (2017). Untangling the annual cycle of the tropical tropopause layer with an idealized moist model [Software]. *Journal of Climate*, *30*(18), 7339–7358. <https://doi.org/10.1175/JCLI-D-17-0127.1>
- Jucker, M., White, I., & Gerber, E. P. (2020). mjucker/mima: MiMA v2.0 [Software]. *Zenodo*. <https://doi.org/10.5281/zenodo.3984605>
- Krawczyk, B. (2016). Learning from imbalanced data: Open challenges and future directions. *Progress in Artificial Intelligence*, *5*(4), 221–232. <https://doi.org/10.1007/s13748-016-0094-0>
- Liaw, R., Liang, E., Nishihara, R., Moritz, P., Gonzalez, J. E., & Stoica, I. (2018). Tune: A research platform for distributed model selection and training. *arXiv preprint arXiv:1807.05118*. <https://arxiv.org/abs/1807.05118>
- Lindzen, R. S. (1981). Turbulence and stress owing to gravity wave and tidal breakdown. *Journal of Geophysical Research*, *86*(C10), 9707–9714. <https://doi.org/10.1029/jc086ic10p09707>
- Oksuz, K., Cam, B. C., Kalkan, S., & Akbas, E. (2021). Imbalance problems in object detection: A review. *IEEE Transactions on Pattern Analysis and Machine Intelligence*, *43*(10), 3388–3415. <https://doi.org/10.1109/TPAMI.2020.2981890>
- Paszke, A., Gross, S., Massa, F., Lerer, A., Bradbury, J., Chanan, G., et al. (2019). PyTorch: An imperative style, high-performance deep learning library. *Advances in Neural Information Processing Systems*, *32*.
- Rabel, E., Rüger, R., Govoni, M., & Ehlert, S. (2018). Forpy: A library for Fortran-Python interoperability [Software]. *GitHub*. Retrieved from <https://github.com/ylikx/forpy>
- Richter, J. H., Anstey, J. A., Butchart, N., Kawatani, Y., Meehl, G. A., Osprey, S., & Simpson, I. R. (2020). Progress in simulating the quasi-biennial oscillation in CMIP models. *Journal of Geophysical Research: Atmospheres*, *125*(8), e2019JD032362. <https://doi.org/10.1029/2019jd032362>
- Richter, J. H., Butchart, N., Kawatani, Y., Bushell, A. C., Holt, L., Serva, F., et al. (2022). Response of the quasi-biennial oscillation to a warming climate in global climate models. *Quarterly Journal of the Royal Meteorological Society*, *148*(744), 1490–1518. <https://doi.org/10.1002/qj.3749>
- Rudy, S. H., & Sapsis, T. P. (2023). Output-weighted and relative entropy loss functions for deep learning precursors of extreme events. *Physica D: Nonlinear Phenomena*, *443*, 133570. <https://doi.org/10.1016/j.physd.2022.133570>
- Shaw, T. A., Sigmond, M., Shepherd, T. G., & Scinocca, J. F. (2009). Sensitivity of simulated climate to conservation of momentum in gravity wave drag parameterization. *Journal of Climate*, *22*(10), 2726–2742. <https://doi.org/10.1175/2009jcli2688.1>
- Sun, Y. Q., Hassanzadeh, P., Alexander, M. J., & Kruse, C. G. (2023). Quantifying 3D gravity wave drag in a library of tropical convection-permitting simulations for data-driven parameterizations. *Journal of Advances in Modeling Earth Systems*, *15*(5), e2022MS003585. <https://doi.org/10.1029/2022MS003585>

- Torgo, L., Branco, P., Ribeiro, R. P., & Pfahringer, B. (2015). Resampling strategies for regression. *Expert Systems*, 32(3), 465–476. <https://doi.org/10.1111/exsy.12081>
- Ukkonen, P. (2022). Exploring pathways to more accurate machine learning emulation of atmospheric radiative transfer. *Journal of Advances in Modeling Earth Systems*, 14(4), e2021MS002875. <https://doi.org/10.1029/2021MS002875>
- Webber, R. J., Plotkin, D. A., O'Neill, M. E., Abbot, D. S., & Weare, J. (2019). Practical rare event sampling for extreme mesoscale weather. *Chaos: An Interdisciplinary Journal of Nonlinear Science*, 29(5).
- Yang, M. (2026). yangminah/GWPREbalance: JAMES publication (JAMES) [Software]. *Zenodo*. <https://doi.org/10.5281/zenodo.18451774>
- Yuval, J., O'Gorman, P. A., & Hill, C. N. (2021). Use of neural networks for stable, accurate and physically consistent parameterization of subgrid atmospheric processes with good performance at reduced precision. *Geophysical Research Letters*, 48(6), e2020GL091363. <https://doi.org/10.1029/2020GL091363>